NANO LETTERS
Letter
Cite This: Nano Lett. 2019, 19, 3091−3097
pubs.acs.org/NanoLett

# Ultrafast Electron Dynamics in Single Aluminum Nanostructures

Man-Nung Su,[†,‡] Christopher J. Ciccarino,[#,▽] Sushant Kumar,[○] Pratiksha D. Dongare,[‡,§,∥] Seyyed Ali Hosseini Jebeli,[‡,∥] David Renard,[†,‡] Yue Zhang,[‡,§,∥] Behnaz Ostovar,[‡,∥] Wei-Shun Chang,[†,‡,¶] Peter Nordlander,[*,‡,∥,⊥] Naomi J. Halas,[*,†,‡,∥,⊥] Ravishankar Sundararaman,[*,○] Prineha Narang,[*,#] and Stephan Link[*,†,‡,∥]

[†]Department of Chemistry, [‡]Laboratory for Nanophotonics, [§]Applied Physics Graduate Program, [∥]Department of Electrical and Computer Engineering, and [⊥]Department of Physics & Astronomy, Rice University, Houston, Texas 77005, United States
[#]John A. Paulson School of Engineering and Applied Sciences and [▽]Department of Chemistry and Chemical Biology, Harvard University, Cambridge, Massachusetts 02138, United States
[○]Department of Materials Science and Engineering, Rensselaer Polytechnic Institute, Troy, New York 12180, United States

Supporting Information

**ABSTRACT:** Aluminum nanostructures are a promising alternative material to noble metal nanostructures for several photonic and catalytic applications, but their ultrafast electron dynamics remain elusive. Here, we combine single-particle transient extinction spectroscopy and parameter-free first-principles calculations to investigate the non-equilibrium carrier dynamics in aluminum nanostructures. Unlike gold nanostructures, we find the sub-picosecond optical response of lithographically fabricated aluminum nanodisks to be more sensitive to the lattice temperature than the electron temperature. We assign the rise in the transient transmission to electron−phonon coupling with a pump-power-independent lifetime of 500 ± 100 fs and theoretically confirm this strong electron−phonon coupling behavior. We also measure electron−phonon lifetimes in chemically synthesized aluminum nanocrystals and find them to be even longer (1.0 ± 0.1 ps) than for the nanodisks. We also observe a rise and decay in the transient transmissions with amplitudes that scale with the surface-to-volume ratio of the aluminum nanodisks, implying a possible hot carrier trapping and detrapping at the native oxide shell−metal core interface.

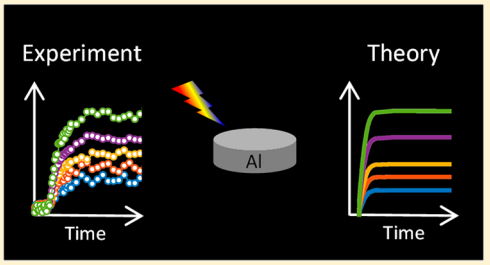


**KEYWORDS:** *Surface plasmon, hot carrier dynamics, ultrafast spectroscopy, single-particle spectroscopy, ab initio calculations*

Metal nanostructures with surface plasmon resonances (SPRs), the collective oscillations of their conduction band electrons, possess large absorption cross-sections, efficient photothermal conversion, strong electric-field enhancement, and high photon energy tunability through particle geometry and environment.[1−4] These highly tunable and strong light−matter interactions are useful in many applications such as catalysts, solar energy converters, lasers, sensors, and biomedical tools.[5−12] Numerous studies on the SPR of noble metal nanostructures have revealed their ultrafast dynamics. The hot electrons generated after SPR excitation are the keys to photocatalysis and solar energy conversion.[13,14] If the hot electrons are not transferred, they cool through electron−phonon relaxation and launch acoustic vibrations, which can be utilized in optomechanical devices at GHz frequencies.[15,16] The energy dissipated from the nanostructures to the surrounding medium via phonon−phonon coupling induces high local temperatures that can be utilized to distill organic solvents[17] and to destroy cancer cells.[18] In such applications, the time scales of hot electron lifetimes and thermal dissipation rates determine efficiency. A fundamental understanding and subsequent control of these processes is, therefore, essential.

Aluminum nanostructures have SPRs tunable from the visible range to the UV, which complements gold and silver nanostructures at shorter wavelengths.[19−25] Aluminum also represents a more sustainable choice than noble metals for scalable applications, given that it is the third most abundant element in the earth's crust. Aluminum nanostructures have already been used in displays,[19,26,27] sensors,[28−32] solar cells,[31,33,34] and photocatalysts.[35−37] A self-terminating surface oxide layer inevitably develops on the surface of aluminum nanostructures when exposed to ambient conditions and affects their SPRs and photocatalytic performance.[20,35,38] Despite the large disparity of the electron−phonon coupling time in aluminum (∼500 fs)[39−42] and gold (a few picoseconds),[43−47] studies on the ultrafast dynamics in zero-dimensional aluminum nanostructures are very limited.[48,49] In particular, a conclusive understanding of the origin of the differential optical response and the effect of the native oxide layer is lacking.

Received: February 3, 2019
Revised: March 21, 2019
Published: April 2, 2019






DOI: 10.1021/acs.nanolett.9b00503
Nano Lett. 2019, 19, 3091−3097

In this work, we investigated the ultrafast dynamics of aluminum nanodisks (AlNDs) using single-particle transient extinction microscopy and ab initio calculations. Unlike gold nanodisks (AuNDs), in which the transient transmission signal for the first few picoseconds arises from dielectric function changes due to high electron temperatures,[50] the transient transmission of AlNDs is caused by the lattice temperature dependence of the dielectric function. Our ab initio calculations confirm this mechanism. An electron−phonon coupling time of 0.5 ps observed in AlNDs is consistent with the results for polycrystalline aluminum thin films.[40] Furthermore, we observed an additional energy relaxation pathway that was not previously observed in thin films and assign it to electron trapping and detrapping at the metal−oxide interfaces.

The transient transmission of AlNDs is distinct from gold nanostructures. AlNDs fabricated by e-beam lithography (see the Supporting Information) were chosen as a well-defined structure and, therefore, as a fair comparison with AuNDs, whose ultrafast dynamics are very well-known.[51,52] Both AlNDs and AuNDs were fabricated with a diameter of 210 nm and a thickness of 35 nm on soda lime glass coverslips (Figure 1a). Transient transmissions were recorded with a

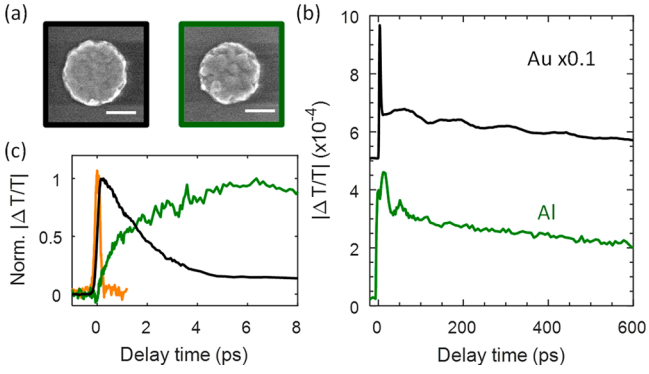


**Figure 1.** Ultrafast dynamics of AuNDs and AlNDs with a diameter of 210 nm and a thickness of 35 nm. (a) SEM images of a AuND (left) and an AlND (right). Scale bars: 100 nm. (b) Transient transmissions of a AuND (black) pumped at 405 nm (fluence of 0.04 mJ/cm$^2$) and probed at 810 nm compared to an AlND (green) pumped at 810 nm (fluence of 0.08 mJ/cm$^2$) and probed at 700 nm. The data is scaled and offset for better visualization. (c) Normalized transient transmissions of a AuND (black) and an AlND (green) shown on a shorter time scale. The orange line is the typical instrument response function (IRF). Its full width at half-maximum (fwhm) was 250−400 fs depending on the use of a reflective vs transmissive objective.

home-built single-particle transient extinction spectrometer (see the Supporting Information and Figure S1). To equally pump the interband transitions and probe at the SPR, the pump and probe wavelengths were 405 and 810 nm for AuNDs and 810 and 700 nm for AlNDs, respectively.[49] The comparison between the transient transmissions of the AlNDs and AuNDs reveals three different traits in AlNDs (Figure 1b). First, in gold nanostructures, the sharp rise and decay (black line, Figure 1c) correspond to electron−electron and electron−phonon scattering, respectively, with lifetimes that are consistent with the lifetimes measured in bulk metals. Considering the bulk electron−electron (~500 fs for gold[53] and ~200 fs for aluminum)[54] and electron−phonon lifetimes (approximately a few picoseconds for gold[43−47] and ~500 fs for aluminum),[40] an even sharper rise and decay are expected for AlNDs. However, a slower rise (green line, Figure 1c) was observed instead. Second, acoustic vibrations with a higher vibration frequency and shorter damping time were observed in AlNDs compared to AuNDs with the same geometry. The acoustic vibrations of AlNDs have been previously reported and explained.[49] Third, in gold nanostructures, the decay following electron−phonon coupling is assigned to thermal relaxation to the environment and can be fit with a single exponential decay.[55] However, in AlNDs we observed a second decay component of 30 ps (green line, Figure 1b). Here, we study the slower rise and 30 ps decay.

To understand the sub-picoseconds dynamics of the transient transmission of AlNDs, we performed ab initio calculations in conjunction with finite difference time domain (FDTD) simulations (see the Supporting Information). We use density-functional theory to describe the electron and phonon properties of aluminum and resolve electron−electron and electron−phonon interactions diagrammatically[56−59] by use of maximally localized Wannier functions.[60] As described in previous work,[46,61] we incorporate these interactions to determine the complex dielectric function, which is then evolved with time by solving the nonlinear Boltzmann equation for the carrier distribution $f(\varepsilon)$. We determine the initial distribution of carriers at time $t = 0$ following an optical excitation as:

$$f(\varepsilon, t = 0) = f_0(\varepsilon) + U\frac{P(\varepsilon, \hbar\omega)}{g(\varepsilon)} \quad (1)$$

for a room-temperature Fermi distribution $f_0(\varepsilon)$, electronic density of states $g(\varepsilon)$, and carrier distribution $P(\varepsilon,\hbar\omega)$ corresponding to carrier energy $\varepsilon$ and photon energy $\hbar\omega$. The parameter $U$ represents the laser pump pulse energy density, which is the only value taken from experiment. In evolving this distribution, we correspondingly evolve the dielectric function with time.

These time-dependent dielectric functions were then used in FDTD simulations that also considered the overall AlND geometry, including the native oxide layer and the glass substrate, to calculate the time-dependent extinction cross-sections, as shown in Figure 2a. Bleaching (increased transmission) and induced extinction (decreased transmission) are predicted for the SPR (500−750 nm) and interband transitions (750−880 nm), respectively. Experimentally, we varied the probe wavelength with 50 nm steps. Probe wavelengths of 800 and 750 nm were avoided due to spectral overlap with the pump wavelength and insufficient differential signal, consistent with the theoretical spectra (Figure 2a). Good agreement is reached between the theoretical and experimental transient transmissions (Figure 2b) in terms of spectral shape considering the positions and relative amplitudes of the bleach and induced extinction. These results therefore justify the direct comparison between the theoretical and experimental data.

The theoretical time evolution of the transient extinction reveals that the rise in the signal of AlNDs is determined by the lattice temperature and electron−phonon coupling. The time dependence of the differential extinction at 700 nm is plotted in Figure 2c. The change in extinction reaches a plateau at about 500 fs after the thermalization between excited electrons and the lattice. We verify these results with our ab initio predictions of both lattice and electron temperature. The lattice temperature $T_l$ is determined by energy balance, in


DOI: 10.1021/acs.nanolett.9b00503
Nano Lett. 2019, 19, 3091−3097

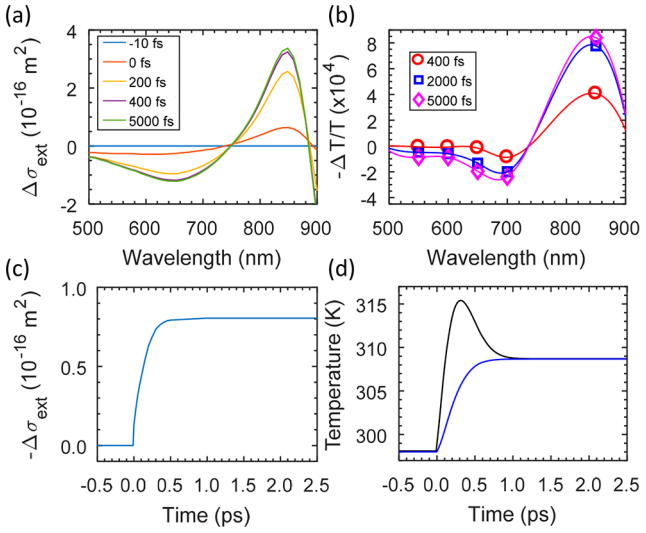


**Figure 2.** Theoretical optical response of AlNDs with a diameter of 210 nm and a thickness of 35 nm pumped at 800 nm with a fluence of 0.08 mJ/cm$^2$. (a) Theoretical transient differential extinction at different delay times as indicated in the legend. (b) Experimental transient transmission at different delay times as indicated in the legend. Lines are cubic spline interpolations as a guide. (c) Theoretical transient differential extinction probed at 700 nm. (d) Temporal evolutions of the theoretical lattice (blue) and electron (black) temperatures determined via eqs 2 and 3

which we assume the phonons remain thermal at all times such that the system obeys the condition:

$$-C_l(T_l)\frac{dT_l}{dt} = \frac{dE}{dt}\Big|_{e-ph} \quad (2)$$

Here, $C_l(T_l)$ is the ab initio lattice heat capacity,[61] and $dE/dt$ represents the rate of enery transfer from the lattice to the electrons as a result of electron−phonon interactions.

The electronic temperature is not a parameter in our model, as we do not assume a unique temperature or distribution profile. However, we can generate a temperature $T_e$ by assuming that the carrier distribution can be described by a Fermi function, which defines the temperature as:

$$T_e(t) = \frac{1}{4k_B}\left(\frac{\partial f(\varepsilon, t)}{\partial \varepsilon}\right)^{-1}_{\varepsilon=\varepsilon_F} \quad (3)$$

where the derivative is evaluated at the Fermi energy $\varepsilon_F$. $k_B$ is the Boltzmann constant. Figure 2d shows the predicted temporal evolution of the electron and lattice temperatures.

While it is generally accepted that the maximum electron temperature is reached before significant electron−phonon thermalization starts in gold,[52] this picture clearly is invalid for aluminum due to stronger electron−phonon coupling. The electron and lattice temperatures instead increase together. The direct comparison between optical response (Figure 2c) and temperature evolution (Figure 2d) demonstrates that the transient transmission of AlNDs follows the trend of the lattice temperature, unlike AuNDs, whose optical response tracks the electron temperature evolution.[52] This behavior results from the fact that aluminum is a Drude-like metal, and therefore, the electron temperature has little effect on the electron density of states.[61,62] This comparison further establishes that the rise of the transient transmission in AlNDs corresponds to electron−phonon coupling.

While the pump-power dependence of measured electron−phonon coupling times is an important characteristic in gold,[52,63] we observed pump-power-independent electron−phonon coupling in AlNDs. In both experiment and theory, the signal intensities scale with the pump power due to higher maximum lattice temperatures (Figure 3a,b). Nevertheless,

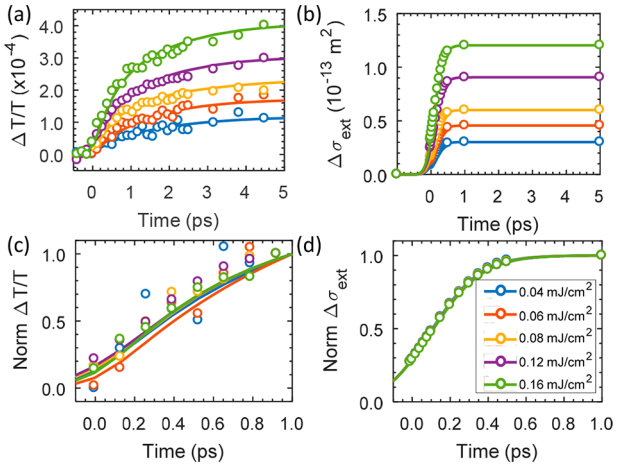


**Figure 3.** Pump-power-dependent transient extinction of AlNDs with a diameter of 210 nm and a thickness of 35 nm probed at 700 nm and pumped at 800 nm with fluences of 0.04 (blue), 0.06 (orange), 0.08 (yellow), 0.12 (purple), and 0.16 (green) mJ/cm$^2$. Panels a and b show absolute experimental and theoretical values, respectively, while panels c and d focus on the early time scale dynamics normalized to the amplitude at 1 ps, illustrating the absence of a pump-power dependence of the rise times. $\Delta T/T$: change in differential transmission. Norm: normalized. $\Delta\sigma_{ext}$: change in extinction cross-section. For all panels, the symbols and solid lines are data points and fits based on a convolution between a Gaussian IRF and a (a, c) bi- or (b, d) mono-exponential rise, respectively.

neither normalized experimental and theoretical data show any dependence on the pump power (Figure 3c,d), which is different from the pump-power-dependent electron−phonon coupling seen in gold (see the Supporting Information and Figure S2). The pump-power dependence in gold results from the fact that the electron heat capacity scales with electron temperature but the electron−phonon coupling constant does not change.[61,64] The electron−phonon lifetimes in aluminum do not change in the range of pump powers used here because of the larger electron−phonon coupling strength, which quickly results in complete electron−phonon thermalization (irrespective of the used pump power).

The experimental electron−phonon coupling time of AlNDs is determined to be 500 ± 100 fs. To obtain the experimental rise times, we fitted the experimental transmissions as a convolution between a Gaussian function and two exponential components. The Gaussian function was included to address the pulse width with a fwhm determined by the cross-correlation between the pump and probe pulses at the sample (instrument response function (IRF), orange line in Figure 1b). A pair of exponential terms were required to achieve a reasonable fit with the experimental data (see the Supporting Information and Figure S3). The two lifetimes were determined to be 500 ± 100 fs and 1.6 ± 0.3 ps. However, only one exponential rise, corresponding to electron−phonon coupling, was observed in the calculated traces. The theoretical differential extinction was first convoluted with a Gaussian



DOI: 10.1021/acs.nanolett.9b00503
Nano Lett. 2019, 19, 3091−3097

function having the same fwhm as the experiment and then was fitted in the same manner but considering only a mono-exponential rise. In this way, the large nonzero signal at time zero could be properly treated (see the Supporting Information and Figure S4).

We determine the theoretical electron–phonon coupling time to be 120 fs, which is shorter than both of the experimental values. Because the faster experimental lifetime matches the experimental value (550 ± 80 fs) obtained for electron–phonon coupling in polycrystalline aluminum films,[40] the experimental fast rise is still assigned to electron–phonon coupling. The slower rise with a lifetime of 1.6 ps is discussed below. The cause of the discrepancy between the experimental and predicted electron–phonon lifetimes is not clear at this moment. More parameters may need to be considered in the ab initio calculation. Some obvious differences between the experiment and theoretical model, such as crystallinity, structural defects, core oxide content, oxide shell, and substrate should in principle lead to shorter lifetimes for the electron–phonon coupling.[65] Further investigations are needed to resolve this discrepancy. Nevertheless the magnitude of the electron–phonon coupling time (hundreds of femtoseconds, Figure 3), spectral shape (Figure 2a,b), and pump power independence of the transient transmission (Figure 3) all match well between experiment and theory.

An even longer electron–phonon coupling time is found in aluminum nanocrystals (AlNCs). AlNCs were chemically synthesized[66] with a diameter of 172 ± 23 nm and measured by transient extinction spectroscopy (Figure 4). While again a

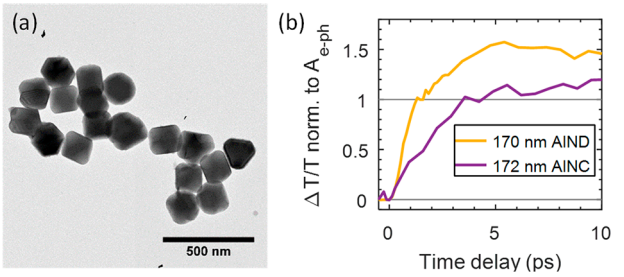


**Figure 4.** Ultrafast electron dynamics of colloidal AlNCs. (a) TEM image of AlNCs. Scale bar: 500 nm. (b) Average transient transmissions of 5 AlNDs (yellow) and 5 AlNCs (purple) with diameters of ~170 nm pumped at 820 nm (fluence: 0.08 mJ/cm$^2$) and probed at 700 nm. The amplitudes were normalized to the amplitude of the fast rise.

bi-exponential rise of the transient transmission is seen, a longer electron–phonon coupling time of 1.0 ± 0.1 ps is obtained for AlNCs. The longer lifetime is expected based on the mono-crystalline nature of AlNCs as the defects in polycrystalline metallic structures reduce the electron–phonon coupling time by increasing the number of collisions.[67] This observation elucidates the importance of mono-crystallinity in aluminum nanostructures for creating longer hot carrier lifetimes.

We assign the experimentally observed 1.5 ps rise and 30 ps decay to electron trapping and detrapping at the core–shell interface. These lifetimes are neither observed in gold nanostructures and aluminum films nor predicted in theory. We studied their size dependence and found that, while the lifetimes do not change, the relative ratio of the slow to the fast rise times and the 30 ps decay compared to the slow thermal relaxation increase for smaller AlND sizes (Figure 5a,b). We propose that the 1.5 ps rise and 30 ps decay correspond to the

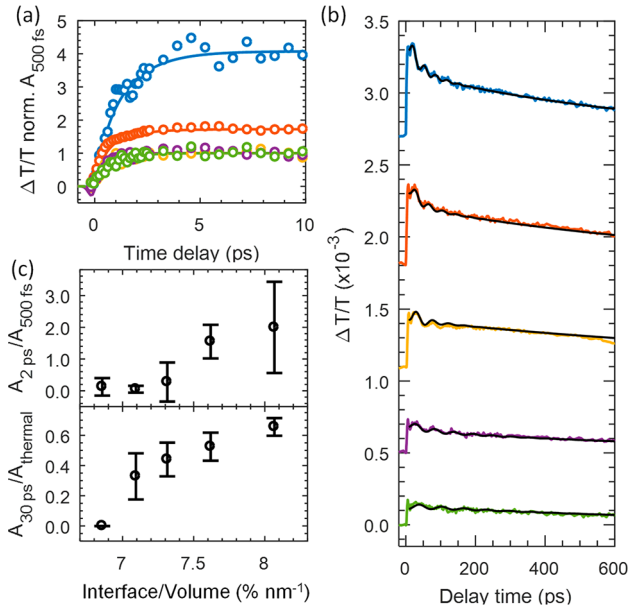


**Figure 5.** Size dependence of the experimental rise and decay of the transient transmission in AlNDs. (a) Transient transmissions normalized to the amplitude of the initial 500 fs rise component for AlNDs with diameters of 170 (blue), 210 (orange), 250 (yellow), 290 (purple), and 350 (green) nm. Pump and probe wavelengths were 810 and 700 nm. The pump fluence was 0.08 mJ/cm$^2$. Circles: data points. Solid lines: fits based on a convolution between a Gaussian IRF and a bi-exponential rise. (b) Single-particle transient transmissions of AlNDs. Pump and probe wavelengths were 810 and 650 nm. The pump energy was 0.10 mJ/cm$^2$. Offsets are added for better visualization. Colored lines: data with diameters as indicated in (a). Black lines: fits to biexponential decays and a damped sine wave to account for the acoustic vibrations. (c) Amplitude ratios of the two rise times (top) and two decay components (bottom) as a function of the ratio between oxide shell–metal core interface area and metal core volume. Error bars are the standard deviations over five independent particles.

trapping and detrapping of excited electrons for the following reasons: (1) smaller AlNDs possess larger interface-to-volume ratios (Figure 5c) as the native oxide layer is approximately 3 nm regardless of nanostructure geometry;[20,35] (2) these additional lifetimes are not observed in gold nanostructures, aluminum films, and the ab initio calculations, in which a native oxide layer does not exist or is less important; and (3) hot electron transport through the oxide layer has been reported.[38] We attempted to understand the origin of the 30 ps decay component with several control experiments. The lifetimes and amplitude ratios were shown to be independent of probe wavelength, core oxide content, and pump power and wavelength (Figures S5–S7). Additionally, adding an oxide interface layer to AuNDs did not cause the additional rise and decay (Figure S8) either. Future theoretical studies of interfacial electronic states may provide more insight into the details of the assigned carrier-trapping mechanism.

Combining single-particle transient extinction spectroscopy and ab initio calculations, we investigated the ultrafast electron dynamics in aluminum nanostructures. Excitation-power-independent electron–phonon relaxation times were observed in both experiments and calculations. The calculations further



DOI: 10.1021/acs.nanolett.9b00503
Nano Lett. 2019, 19, 3091–3097

show that the transient optical response, unlike for gold nanostructures, is dominated by the change in lattice temperature instead of electron temperature. We determined an experimental electron−phonon coupling time of 500 fs for AlNDs, which is consistent with polycrystalline aluminum films. Mono-crystalline AlNCs possess longer electron−phonon coupling times of about 1 ps. We also observed an additional rise and decay in the experimental transient transmissions with lifetimes of 1.5 and 30 ps, respectively, which we assign to the trapping and detrapping of excited charge carriers at the metal core−oxide shell interface, creating the possibility of elongating hot carrier lifetimes with the oxide layer.

## ■ ASSOCIATED CONTENT

### Supporting Information

The Supporting Information is available free of charge on the ACS Publications website at DOI: 10.1021/acs.nanolett.9b00503.

Sample preparation and characterization, single-particle transient extinction microscopy, pump-power dependence in AuNDs, ab initio methods, FDTD simulations, data analysis, and additional data for the 30 ps decay component (PDF)

## ■ AUTHOR INFORMATION


### Corresponding Authors

*E-mail: slink@rice.edu; phone: (713) 348-4561.
*E-mail: prineha@seas.harvard.edu; phone: (617) 496-4710.
*E-mail: sundar@rpi.edu; phone: (518) 276-6757.
*E-mail: halas@rice.edu; phone: (713) 348-5746.
*E-mail: nordland@rice.edu; phone: (713) 348-5171.

### ORCID

Man-Nung Su: 0000-0003-2570-4285
David Renard: 0000-0002-1917-679X
Wei-Shun Chang: 0000-0002-0251-4449
Peter Nordlander: 0000-0002-1633-2937
Naomi J. Halas: 0000-0002-8461-8494
Ravishankar Sundararaman: 0000-0002-0625-4592
Stephan Link: 0000-0002-4781-930X

### Present Address

¶Department of Chemistry and Biochemistry, University of Massachusetts Dartmouth, 285 Old Westport Road, North Dartmouth, MA 02747, United States


### Author Contributions

The manuscript was written through contributions of all authors. All authors have given approval to the final version of the manuscript. C. J. Ciccarino and S. Kumar contributed equally.

### Notes

The authors declare no competing financial interest.

## ■ ACKNOWLEDGMENTS

P. Nordlander, N. J. Halas, and S. Link thank the Robert A. Welch Foundation (grant nos. C-1220 to N. J. Halas, C-1222 to P. Nordlander, and C-1664 to S. Link) and the Air Force Office of Scientific Research via the Department of Defense Multidisciplinary University Research Initiative, under award FA9550-15-1-0022 for financial support. S. Link acknowledges support from the National Science Foundation (ECCS-1608917). R. Sundararaman acknowledges startup funding from the Department of Materials Science and Engineering at Rensselaer Polytechnic Institute. P. Narang acknowledges support from the STC Center for Integrated 356 Quantum Materials NSF grant no. DMR-1231319 and from the Army Research Office MURI (Ab-Initio Solid-State Quantum Materials) grant number W911NF-18-1- 0431. C. Ciccarino is supported by the Army Research Office MURI (Ab-Initio Solid-State Quantum Materials) grant number W911NF-18-1-0431. This research used resources of the National Energy Research Scientific Computing Center, a DOE Office of Science User Facility supported by the Office of Science of the U.S. Department of Energy under contract no. DE-AC02-05CH11231, as well as resources at the BlueGene/Q supercomputer in the Center for Computational Innovations (CCI) at Rensselaer Polytechnic Institute and Research Computing Group at Harvard University. D. Renard was supported by the Department of Defense (DoD) through the National Defense Science & Engineering Graduate Fellowship (NDSEG) Program. We thank Dr. Kyle W. Smith for help with editing the manuscript.

## ■ REFERENCES


(1) Willets, K. A.; Van Duyne, R. P. Localized surface plasmon resonance spectroscopy and sensing. *Annu. Rev. Phys. Chem.* **2007**, *58*, 267−297.
(2) Kelly, K. L.; Coronado, E.; Zhao, L. L.; Schatz, G. C. The Optical Properties of Metal Nanoparticles: The Influence of Size, Shape, and Dielectric Environment. *J. Phys. Chem. B* **2003**, *107*, 668−677.
(3) Lal, S.; Link, S.; Halas, N. J. Nano-optics from sensing to waveguiding. *Nat. Photonics* **2007**, *1*, 641−648.
(4) Halas, N. J.; Lal, S.; Chang, W. S.; Link, S.; Nordlander, P. Plasmons in Strongly Coupled Metallic Nanostructures. *Chem. Rev.* **2011**, *111*, 3913−3961.
(5) Zhang, Y.; He, S.; Guo, W.; Hu, Y.; Huang, J.; Mulcahy, J. R.; Wei, W. D. Surface-Plasmon-Driven Hot Electron Photochemistry. *Chem. Rev.* **2018**, *118*, 2927−2954.
(6) Brongersma, M. L.; Halas, N. J.; Nordlander, P. Plasmon-induced hot carrier science and technology. *Nat. Nanotechnol.* **2015**, *10*, 25.
(7) Ueno, K.; Oshikiri, T.; Sun, Q.; Shi, X.; Misawa, H. Solid-State Plasmonic Solar Cells. *Chem. Rev.* **2018**, *118*, 2955−2993.
(8) Wang, D.; Wang, W.; Knudson, M. P.; Schatz, G. C.; Odom, T. W. Structural Engineering in Plasmon Nanolasers. *Chem. Rev.* **2018**, *118*, 2865−2881.
(9) Mayer, K. M.; Hafner, J. H. Localized Surface Plasmon Resonance Sensors. *Chem. Rev.* **2011**, *111*, 3828−3857.
(10) Jiang, N.; Zhuo, X.; Wang, J. Active Plasmonics: Principles, Structures, and Applications. *Chem. Rev.* **2018**, *118*, 3054−3099.
(11) Lim, W. Q.; Gao, Z. Plasmonic nanoparticles in biomedicine. *Nano Today* **2016**, *11*, 168−188.
(12) Cheng, L.; Wang, C.; Feng, L.; Yang, K.; Liu, Z. Functional Nanomaterials for Phototherapies of Cancer. *Chem. Rev.* **2014**, *114*, 10869−10939.
(13) Thomann, I.; Pinaud, B. A.; Chen, Z.; Clemens, B. M.; Jaramillo, T. F.; Brongersma, M. L. Plasmon Enhanced Solar-to-Fuel Energy Conversion. *Nano Lett.* **2011**, *11*, 3440−3446.
(14) Atwater, H. A.; Polman, A. Plasmonics for improved photovoltaic devices. *Nat. Mater.* **2010**, *9*, 205−213.
(15) Zharov, V. P. Ultrasharp nonlinear photothermal and photoacoustic resonances and holes beyond the spectral limit. *Nat. Photonics* **2011**, *5*, 110−116.
(16) Lin, K.-H.; Lai, C.-M.; Pan, C.-C.; Chyi, J.-I.; Shi, J.-W.; Sun, S.-Z.; Chang, C.-F.; Sun, C.-K. Spatial manipulation of nanoacoustic waves with nanoscale spot sizes. *Nat. Nanotechnol.* **2007**, *2*, 704−708.




DOI: 10.1021/acs.nanolett.9b00503
*Nano Lett.* 2019, 19, 3091−3097

(17) Neumann, O.; Neumann, A. D.; Silva, E.; Ayala-Orozco, C.; Tian, S.; Nordlander, P.; Halas, N. J. Nanoparticle-Mediated, Light-Induced Phase Separations. *Nano Lett.* **2015**, *15*, 7880−7885.
(18) Lukianova-Hleb, E. Y.; Ren, X.; Sawant, R. R.; Wu, X.; Torchilin, V. P.; Lapotko, D. O. On-demand intracellular amplification of chemoradiation with cancer-specific plasmonic nanobubbles. *Nat. Med.* **2014**, *20*, 778.
(19) Olson, J.; Manjavacas, A.; Liu, L.; Chang, W.-S.; Foerster, B.; King, N. S.; Knight, M. W.; Nordlander, P.; Halas, N. J.; Link, S. Vivid, full-color aluminum plasmonic pixels. *Proc. Natl. Acad. Sci. U. S. A.* **2014**, *111*, 14348−14353.
(20) Knight, M. W.; King, N. S.; Liu, L.; Everitt, H. O.; Nordlander, P.; Halas, N. J. Aluminum for Plasmonics. *ACS Nano* **2014**, *8*, 834−840.
(21) Langhammer, C.; Schwind, M.; Kasemo, B.; Zorić, I. Localized Surface Plasmon Resonances in Aluminum Nanodisks. *Nano Lett.* **2008**, *8*, 1461−1471.
(22) McMahon, J. M.; Schatz, G. C.; Gray, S. K. Plasmonics in the ultraviolet with the poor metals Al, Ga, In, Sn, Tl, Pb, and Bi. *Phys. Chem. Chem. Phys.* **2013**, *15*, 5415−5423.
(23) Taguchi, A.; Saito, Y.; Watanabe, K.; Yijian, S.; Kawata, S. Tailoring plasmon resonances in the deep-ultraviolet by size-tunable fabrication of aluminum nanostructures. *Appl. Phys. Lett.* **2012**, *101*, 081110.
(24) Ekinci, Y.; Solak, H. H.; Löffler, J. F. Plasmon resonances of aluminum nanoparticles and nanorods. *J. Appl. Phys.* **2008**, *104*, 083107.
(25) Zorić, I.; Zäch, M.; Kasemo, B.; Langhammer, C. Gold, Platinum, and Aluminum Nanodisk Plasmons: Material Independence, Subradiance, and Damping Mechanisms. *ACS Nano* **2011**, *5*, 2535−2546.
(26) Tan, S. J.; Zhang, L.; Zhu, D.; Goh, X. M.; Wang, Y. M.; Kumar, K.; Qiu, C.-W.; Yang, J. K. W. Plasmonic Color Palettes for Photorealistic Printing with Aluminum Nanostructures. *Nano Lett.* **2014**, *14*, 4023−4029.
(27) Tseng, M. L.; Yang, J.; Semmlinger, M.; Zhang, C.; Nordlander, P.; Halas, N. J. Two-Dimensional Active Tuning of an Aluminum Plasmonic Array for Full-Spectrum Response. *Nano Lett.* **2017**, *17*, 6034−6039.
(28) Besteiro, L. V.; Zhang, H.; Plain, J.; Markovich, G.; Wang, Z.; Govorov, A. O. Aluminum Nanoparticles with Hot Spots for Plasmon-Induced Circular Dichroism of Chiral Molecules in the UV Spectral Interval. *Adv. Opt. Mater.* **2017**, *5*, 1700069.
(29) McPeak, K. M.; van Engers, C. D.; Bianchi, S.; Rossinelli, A.; Poulikakos, L. V.; Bernard, L.; Herrmann, S.; Kim, D. K.; Burger, S.; Blome, M.; Jayanti, S. V.; Norris, D. J. Ultraviolet Plasmonic Chirality from Colloidal Aluminum Nanoparticles Exhibiting Charge-Selective Protein Detection. *Adv. Mater.* **2015**, *27*, 6244−6250.
(30) Jha, S. K.; Ahmed, Z.; Agio, M.; Ekinci, Y.; Löffler, J. F. Deep-UV Surface-Enhanced Resonance Raman Scattering of Adenine on Aluminum Nanoparticle Arrays. *J. Am. Chem. Soc.* **2012**, *134*, 1966−1969.
(31) Xu, Q.; Liu, F.; Liu, Y.; Meng, W.; Cui, K.; Feng, X.; Zhang, W.; Huang, Y. Aluminum plasmonic nanoparticles enhanced dye sensitized solar cells. *Opt. Express* **2014**, *22*, A301−A310.
(32) Ayas, S.; Topal, A. E.; Cupallari, A.; Güner, H.; Bakan, G.; Dana, A. Exploiting Native Al2O3 for Multispectral Aluminum Plasmonics. *ACS Photonics* **2014**, *1*, 1313−1321.
(33) Kochergin, V.; Neely, L.; Jao, C.-Y.; Robinson, H. D. Aluminum plasmonic nanostructures for improved absorption in organic photovoltaic devices. *Appl. Phys. Lett.* **2011**, *98*, 133305.
(34) Sygletou, M.; Kakavelakis, G.; Paci, B.; Generosi, A.; Kymakis, E.; Stratakis, E. Enhanced Stability of Aluminum Nanoparticle-Doped Organic Solar Cells. *ACS Appl. Mater. Interfaces* **2015**, *7*, 17756−17764.
(35) Zhou, L.; Zhang, C.; McClain, M. J.; Manjavacas, A.; Krauter, C. M.; Tian, S.; Berg, F.; Everitt, H. O.; Carter, E. A.; Nordlander, P.; Halas, N. J. Aluminum Nanocrystals as a Plasmonic Photocatalyst for Hydrogen Dissociation. *Nano Lett.* **2016**, *16*, 1478−1484.
(36) Hao, Q.; Wang, C.; Huang, H.; Li, W.; Du, D.; Han, D.; Qiu, T.; Chu, P. K. Aluminum plasmonic photocatalysis. *Sci. Rep.* **2015**, *5*, 15288.
(37) Honda, M.; Kumamoto, Y.; Taguchi, A.; Saito, Y.; Kawata, S. Efficient UV photocatalysis assisted by densely distributed aluminum nanoparticles. *J. Phys. D: Appl. Phys.* **2015**, *48*, 184006.
(38) Robatjazi, H.; Zhao, H.; Swearer, D. F.; Hogan, N. J.; Zhou, L.; Alabastri, A.; McClain, M. J.; Nordlander, P.; Halas, N. J. Plasmon-induced selective carbon dioxide conversion on earth-abundant aluminum-cuprous oxide antenna-reactor nanoparticles. *Nat. Commun.* **2017**, *8*, 27.
(39) Richardson, C. J. K.; Spicer, J. B. Short-time thermoelastic contributions to picosecond-time scale reflectivity measurements of metals. *Appl. Phys. Lett.* **2002**, *80*, 2895−2897.
(40) Nie, S.; Wang, X.; Park, H.; Clinite, R.; Cao, J. Measurement of the Electronic Gruneisen Constant Using Femtosecond Electron Diffraction. *Phys. Rev. Lett.* **2006**, *96*, 025901.
(41) Hostetler, J. L.; Smith, A. N.; Czajkowsky, D. M.; Norris, P. M. Measurement of the electron-phonon coupling factor dependence on film thickness and grain size in Au, Cr, and Al. *Appl. Opt.* **1999**, *38*, 3614−3620.
(42) Guo, C.; Rodriguez, G.; Lobad, A.; Taylor, A. J. Structural Phase Transition of Aluminum Induced by Electronic Excitation. *Phys. Rev. Lett.* **2000**, *84*, 4493−4496.
(43) Arbouet, A.; Voisin, C.; Christofilos, D.; Langot, P.; Fatti, N. D.; Vallée, F.; Lermé, J.; Celep, G.; Cottancin, E.; Gaudry, M.; Pellarin, M.; Broyer, M.; Maillard, M.; Pileni, M. P.; Treguer, M. Electron-Phonon Scattering in Metal Clusters. *Phys. Rev. Lett.* **2003**, *90*, 177401.
(44) Hohlfeld, J.; Wellershoff, S. S.; Güdde, J.; Conrad, U.; Jähnke, V.; Matthias, E. Electron and lattice dynamics following optical excitation of metals. *Chem. Phys.* **2000**, *251*, 237−258.
(45) Tas, G.; Maris, H. J. Electron diffusion in metals studied by picosecond ultrasonics. *Phys. Rev. B: Condens. Matter Mater. Phys.* **1994**, *49*, 15046−15054.
(46) Brown, A. M.; Sundararaman, R.; Narang, P.; Schwartzberg, A. M.; Goddard, W. A.; Atwater, H. A. Experimental and Ab Initio Ultrafast Carrier Dynamics in Plasmonic Nanoparticles. *Phys. Rev. Lett.* **2017**, *118*, 087401.
(47) Sun, C. K.; Vallée, F.; Acioli, L. H.; Ippen, E. P.; Fujimoto, J. G. Femtosecond-tunable measurement of electron thermalization in gold. *Phys. Rev. B: Condens. Matter Mater. Phys.* **1994**, *50*, 15337−15348.
(48) Smith, K. J.; Cheng, Y.; Arinze, E. S.; Kim, N. E.; Bragg, A. E.; Thon, S. M. Dynamics of Energy Transfer in Large Plasmonic Aluminum Nanoparticles. *ACS Photonics* **2018**, *5*, 805−813.
(49) Su, M.-N.; Dongare, P. D.; Chakraborty, D.; Zhang, Y.; Yi, C.; Wen, F.; Chang, W.-S.; Nordlander, P.; Sader, J. E.; Halas, N. J.; Link, S. Optomechanics of Single Aluminum Nanodisks. *Nano Lett.* **2017**, *17*, 2575−2583.
(50) Voisin, C.; Del Fatti, N.; Christofilos, D.; Vallee, F. Ultrafast Electron Dynamics and Optical Nonlinearities in Metal Nanoparticles. *J. Phys. Chem. B* **2001**, *105*, 2264−2280.
(51) Chang, W.-S.; Wen, F.; Chakraborty, D.; Su, M.-N.; Zhang, Y.; Shuang, B.; Nordlander, P.; Sader, J. E.; Halas, N. J.; Link, S. Tuning the acoustic frequency of a gold nanodisk through its adhesion layer. *Nat. Commun.* **2015**, *6*, 7022.
(52) Hartland, G. V. Optical Studies of Dynamics in Noble Metal Nanostructures. *Chem. Rev.* **2011**, *111*, 3858−3887.
(53) Del Fatti, N.; Bouffanais, R.; Vallée, F.; Flytzanis, C. Nonequilibrium Electron Interactions in Metal Films. *Phys. Rev. Lett.* **1998**, *81*, 922−925.
(54) Rethfeld, B.; Kaiser, A.; Vicanek, M.; Simon, G. Ultrafast dynamics of nonequilibrium electrons in metals under femtosecond laser irradiation. *Phys. Rev. B: Condens. Matter Mater. Phys.* **2002**, *65*, 214303.
(55) Zijlstra, P.; Tchebotareva, A. L.; Chon, J. W. M.; Gu, M.; Orrit, M. Acoustic oscillations and elastic moduli of single gold nanorods. *Nano Lett.* **2008**, *8*, 3493−3497.


DOI: 10.1021/acs.nanolett.9b00503
*Nano Lett.* 2019, 19, 3091−3097

(56) Brown, A. M.; Sundararaman, R.; Narang, P.; Goddard, W. A., III; Atwater, H. A. Nonradiative plasmon decay and hot carrier dynamics: effects of phonons, surfaces, and geometry. *ACS Nano* **2016**, *10*, 957−966.
(57) Ravishankar Sundararaman, T. C.; Christensen, T.; Ping, Y.; Rivera, N.; Joannopoulos, J. D.; Soljacic, M.; Narang, P. Plasmonics in Argentene. arXiv.org e-Print Archive. *arXiv:1806.02672* (accessed).
(58) Ciccarino, C. J.; Christensen, T.; Sundararaman, R.; Narang, P. Dynamics and Spin-Valley Locking Effects in Monolayer Transition Metal Dichalcogenides. *Nano Lett.* **2018**, *18*, 5709−5715.
(59) Coulter, J.; Sundararaman, R.; Narang, P. Microscopic origins of hydrodynamic transport in the type-II Weyl semimetal $WP_2$. *Phys. Rev. B: Condens. Matter Mater. Phys.* **2018**, *98*, 115130.
(60) Souza, I.; Marzari, N.; Vanderbilt, D. Maximally localized Wannier functions for entangled energy bands. *Phys. Rev. B: Condens. Matter Mater. Phys.* **2001**, *65*, 035109.
(61) Brown, A. M.; Sundararaman, R.; Narang, P.; Goddard, W. A., III; Atwater, H. A. Ab initio phonon coupling and optical response of hot electrons in plasmonic metals. *Phys. Rev. B: Condens. Matter Mater. Phys.* **2016**, *94*, 075120.
(62) Lin, Z.; Zhigilei, L. V.; Celli, V. Electron-phonon coupling and electron heat capacity of metals under conditions of strong electron-phonon nonequilibrium. *Phys. Rev. B: Condens. Matter Mater. Phys.* **2008**, *77*, 075133.
(63) Link, S.; El-Sayed, M. A. Spectral properties and relaxation dynamics of surface plasmon electronic oscillations in gold and silver nanodots and nanorods. *J. Phys. Chem. B* **1999**, *103*, 8410−8426.
(64) Del Fatti, N.; Voisin, C.; Achermann, M.; Tzortzakis, S.; Christofilos, D.; Vallée, F. Nonequilibrium electron dynamics in noble metals. *Phys. Rev. B: Condens. Matter Mater. Phys.* **2000**, *61*, 16956−16966.
(65) Allan, G.; Delerue, C. Fast relaxation of hot carriers by impact ionization in semiconductor nanocrystals: Role of defects. *Phys. Rev. B: Condens. Matter Mater. Phys.* **2009**, *79*, 195324.
(66) McClain, M. J.; Schlather, A. E.; Ringe, E.; King, N. S.; Liu, L.; Manjavacas, A.; Knight, M. W.; Kumar, I.; Whitmire, K. H.; Everitt, H. O.; Nordlander, P.; Halas, N. J. Aluminum Nanocrystals. *Nano Lett.* **2015**, *15*, 2751−2755.
(67) Elsayed-Ali, H. E.; Juhasz, T.; Smith, G. O.; Bron, W. E. Femtosecond thermoreflectivity and thermotransmissivity of polycrystalline and single-crystalline gold films. *Phys. Rev. B: Condens. Matter Mater. Phys.* **1991**, *43*, 4488−4491.



DOI: 10.1021/acs.nanolett.9b00503
*Nano Lett.* 2019, 19, 3091−3097